

Linear Mixture Analysis-Based Compression for Hyperspectral Image Analysis

Qian Du, *Member, IEEE*, and Chein-I Chang, *Senior Member, IEEE*

Abstract—Due to significantly improved spectral resolution produced by hyperspectral sensors, the band-to-band correlation is generally very high and can be removed without loss of crucial information. Data compression is an effective means to eliminate such redundancy resulting from high interband correlation. In hyperspectral imagery, various information comes from different signal sources, which include man-made targets, natural backgrounds, unknown clutters, interferers, unidentified anomalies, etc. In many applications, whether or not a compression technique is effective is measured by the degree of information loss rather than information recovery. For example, compression of noise or interferers is highly desirable to image analysis and interpretation. In this paper, we present an unsupervised fully constrained least squares (UFCLS) linear spectral mixture analysis (LSMA)-based compression technique for hyperspectral target detection and classification. Unlike most compression techniques, which deal directly with grayscale images, the proposed compression approach generates and encodes the fractional abundance images of targets of interest present in an image scene to achieve data compression. Since the vital information used for image analysis is generally preserved and retained in these fractional abundance images, the loss of information may have little impact on image analysis. On some occasions, it even improves performance analysis. Airborne Visible/InfraRed Imaging Spectrometer (AVIRIS) and Hyperspectral Digital Imagery Collection Experiment (HYDICE) data are used for experiments to evaluate our proposed LSMA-based compression technique used for applications in hyperspectral detection and image classification. The classification results using the original data and the UFCLS-decompressed data are shown to be very close with no visible difference. But a compression ratio for the HYDICE data with water bands removed can achieve as high as 138 : 1 with peak SNR (PSNR) 33 dB, while a compression ratio of the AVIRIS scene also with water bands removed is 90 : 1 with PSNR 40 dB.

Index Terms—Fully constrained least squares linear unmixing (FCLSLU), hyperspectral data compression, linear spectral mixture analysis (LSMA), nonnegatively constrained least squares (NCLS), unsupervised fully constrained least squares linear unmixing (UFCLSLU).

Manuscript received January 31, 2002; revised May 30, 2003. This work was supported in part by Bechtel Nevada Corporation under Contract DE-AC08-96NV11718 through the U.S. Department of Energy, in part by the Office of Naval Research under Contract N00014-01-1-0359, in part by the National Research Council under a Senior Research Associateship sponsored by the U.S. Army Soldier and Biological Command, Edgewood Chemical and Biological Center, and in part by an award from the TRW Foundation.

Q. Du is with the Department of Electrical Engineering and Computer Science, Texas A&M University, Kingsville, TX 78363 USA.

C.-I Chang is with the Department of Computer Science and Electrical Engineering, Remote Sensing Signal and Image Processing Laboratory, University of Maryland, Baltimore County, Baltimore, MD 21250 USA.

Digital Object Identifier 10.1109/TGRS.2003.816668

I. INTRODUCTION

WITH VERY HIGH spectral resolution, hyperspectral imagery expands the capability of multispectral imagery in many ways, such as subpixel detection, object discrimination, mixed-pixel classification, and material quantification, etc. However, it also presents new challenges to image analysts, particularly, how to effectively deal with the enormous data volumes while still achieving desired goals. One common practice is to compress data prior to image analysis. For remotely sensed imagery, both lossless compression and lossy compression have been studied and investigated extensively in the past [1]–[8]. In hyperspectral data exploitation, a fundamental task is target/object detection and classification. In military and intelligence applications, man-made targets are most significant objects of interest, but they are also relatively small. As a matter of fact, their occurrence may only appear in a few pixels. If lossy compression is performed without taking these objects into account, these small targets may be suppressed inadvertently. On the other hand, if lossless compression is performed, these targets may survive by compression, but many unknown image background signatures and noise may also be preserved and could further obscure the desired targets. From a target detection and image classification point of view, the performance in detection and classification is generally determined by how we can effectively use features of targets in the image data rather than the entire data. A good example is Fisher's linear discriminant analysis (LDA) [9] that has been widely used in pattern classification. As a result, lossless compression does not provide additional advantages over lossy compression in the sense of feature extraction.

To evaluate the effect of compression, selecting an appropriate criterion for optimality to meet a specific goal is crucial. For example, principal components analysis (PCA), also known as the Karhunen–Loeve transform (KLT), is a commonly used compression technique that represents data in a few principal components by finding projections along the largest data variances [10]–[13]. Unfortunately, it was recently shown in [14]–[16] that the SNR is a better criterion than variance to measure image quality for multispectral imagery. Similarly, mean-squared error (MSE) has been also used as a common criterion for optimality in communications and signal processing, such as quantization. Nevertheless, it is also known that the MSE may not be an appropriate measure for image quality. In hyperspectral imagery, its very high spatial and spectral resolution enables us to reveal many subtle substances, some of which may be very important in image analysis, but their spatial extent can be limited to relatively small areas. If the data variance or the MSE is

used as a compression criterion, these substances may be very likely suppressed and sacrificed.

In this paper, we consider applications as compression criteria. In particular, we are mainly interested in spectral compression rather than spatial compression, and we investigate an application of linear spectral mixture analysis (LSMA) [17], [18] in hyperspectral image compression from a perspective of target detection and classification. The targets referred to here represent the material substances of interest present in image data. Unlike Fisher's LDA, which can be used to compress data from a pattern classification viewpoint, our proposed LSMA-based compression technique is developed based on target detection and classification. To be more specific, in pattern classification, every image pixel must be assigned to one of the pattern classes. It includes classification of background that may not be of interest in applications. In target classification, pattern classes are target classes that are only made up of targets of particular interest such as man-made targets, and the classification is generally performed on these targets without reference to image background. In order to account for such applications, the commonly used compression criteria, e.g., SNR, data variance, and MSE, may not be applicable. Instead, an application-based criterion is more appropriate. One such an application-based approach was suggested in [19], which used an LSMA-based orthogonal projection (OP) filter to compress Airborne Visible/InfraRed Imaging Spectrometer (AVIRIS) data to achieve target classification. The proposed OP filter was based on feature extraction and is the same classifier as proposed in [20], called the orthogonal subspace projection (OSP) classifier. Using the LSMA to compress hyperspectral images can be beneficial because it preserves spectral properties of material substances present in pixels where the abundance fractions of the substances are important features in detection and classification. In this case, dealing directly with these abundance fractions may be more effective than working on the entire hyperspectral image cube. Since the number of material substances is generally much smaller than that of spectral bands, a considerable compression can be always achieved by preserving images that represent substance abundance fractions, referred to as fractional abundance images in this paper. Additionally, such fractional abundance images may be sufficient to provide all necessary information for performance analysis. Unfortunately, the OP filter approach in [19] is an unconstrained LSMA-based linear unmixing method, which did not accurately estimate the substance abundance fractions. Consequently, results obtained by using these abundance fractions as features for compression may be misleading. Similar problems also occur in the approaches proposed in [21] where the filter vector algorithm (FVA) was not abundance-constrained. In order to resolve this problem, two constraints ought to be imposed on the LSMA, which are: 1) the abundance sum-to-one constraint (ASC), where the abundance fractions of all the targets must be summed to one and 2) the abundance nonnegativity constraint (ANC), where the abundance fractions of all the targets must be nonnegative. The resulting LSMA technique is called fully constrained LSMA, which has been studied in the past [22]–[27]. The LSMA-based compression approach proposed in this paper is derived from techniques in [27]. Part of our re-

sults was also reported in [28]. It has two important features: it is a fully constrained LSMA-based compression method and also completely unsupervised. It generates a set of fractional abundance images in an unsupervised manner, and then compresses the image data by only encoding these fractional abundance images. The benefit resulting from such spectral compression is tremendous, because the image background can be significantly compressed, and the resulting variances of fractional abundance images are also substantially reduced. As a consequence, the spatial correlation that still remains is only among target pixels present in these abundance images. Since the population of target pixels of interest is relatively small, very little spatial redundancy needs to be removed. In this case, an entropy coding method such as Huffman coding can effectively remove coding redundancy pixel-by-pixel. A similar approach, referred to as unmixing/wavelet in [13], was also recently investigated, where it used a spectral library and a standard linear unmixing followed by wavelets to compress data and applied anomaly detection as exploitation criterion to the compressed-reconstructed data. Our proposed LSMA-based compression is different from this approach in that it is a fully abundance-constrained linear unmixing method that can be carried out in a completely unsupervised fashion.

The remainder of this paper is organized as follows. Section II briefly describes the LSMA. Section III introduces a fully constrained least squares linear unmixing (FCLSLU) method. Section IV develops an unsupervised FCLSLU (UFCLSLU)-based compression technique for hyperspectral image compression. Section V presents qualitative and quantitative experimental results using HYDICE (Hyperspectral Digital Imagery Collection Experiment) data. Section VI concludes with some remarks.

II. LSMA

Remotely sensed images can be represented by image cubes with the third dimension specified by spectral bands. Therefore, unlike standard spatial-based image processing, remote sensing image processing must deal with spatial as well as spectral information. When data compression is performed for remote sensing imagery, both spatial and spectral redundancy must be considered. Many techniques reported in multispectral/hyperspectral data compression, such as transform coding, PCA, discrete cosine transform, vector quantization, and wavelet transform, etc., have been focused on design of coding techniques rather than on their utility in applications. In many cases, compression can be more effective if applications are specified. This paper takes this approach by considering target detection and classification as criteria for hyperspectral data compression. Our particular interest is to take advantage of the utility of the LSMA [17], [18] in hyperspectral image analysis to compress data. In this case, the information not relevant to targets of interest used in the linear mixture model will be compressed with little impact on the final results. Suppose that L is the number of spectral bands. Let \mathbf{r} be an $L \times 1$ column pixel vector in a multispectral or hyperspectral image, where boldface is used for vectors. Assume that there are p targets of interest, $\mathbf{t}_1, \mathbf{t}_2, \dots, \mathbf{t}_p$ in an image scene. Let \mathbf{M} be an $L \times p$ target signature matrix denoted by $[\mathbf{m}_1 \ \mathbf{m}_2 \ \dots \ \mathbf{m}_p]$, where

\mathbf{m}_j is an $L \times 1$ column vector represented by the signature of the j th target \mathbf{t}_j resident in the pixel \mathbf{r} . Further, assume that $\boldsymbol{\alpha} = (\alpha_1, \alpha_2, \dots, \alpha_p)^T$ is a $p \times 1$ target abundance column vector associated with \mathbf{r} , where α_j denotes the abundance fraction of the j th target signature in \mathbf{r} . A general approach is to model a pixel vector \mathbf{r} as a linear mixture of $\mathbf{m}_1, \mathbf{m}_2, \dots, \mathbf{m}_p$ as follows:

$$\mathbf{r} = \mathbf{M}\boldsymbol{\alpha} + \mathbf{n} \quad (1)$$

where \mathbf{n} is included to account for either a measurement or model error. Here, without confusion, \mathbf{r} will be used to represent either the pixel vector \mathbf{r} or its spectral signature (i.e., digital numbers). The model represented by (1) is a linear regression form, which assumes that the spectral signature \mathbf{r} is linearly mixed by p distinct spectral signatures $\mathbf{m}_1, \mathbf{m}_2, \dots, \mathbf{m}_p$ with unknown mixing coefficients $\alpha_1, \alpha_2, \dots, \alpha_p$. A general approach to solving (or estimating) the unknown mixing coefficients $\alpha_1, \alpha_2, \dots, \alpha_p$ in (1) is linear spectral mixture analysis, where a fractional abundance image is generated by the LSMA for each of the mixing coefficients. In other words, a fractional abundance image is a grayscale image with grayscales representing abundance fractions of a mixing substance that is specified by a particular target present in each image pixel vector. The mixed pixel \mathbf{r} is then classified according to the set of p fractional abundance images generated by the LSMA that correspond to $\alpha_1, \alpha_2, \dots, \alpha_p$. By virtue of these p fractional abundance images, we can compress the image data by encoding each image pixel vector \mathbf{r} using its corresponding abundance vector $\boldsymbol{\alpha}$ rather than the image pixel vector \mathbf{r} itself. As a result, the original L -band hyperspectral image cube can be represented by these p two-dimensional (2-D) fractional abundance images. Since p is usually much smaller than L in hyperspectral imagery, a significant compression can be achieved. In addition, if the estimated abundance vector $\boldsymbol{\alpha}$ can faithfully represent an image pixel vector \mathbf{r} , the loss of information will be immaterial and have little impact on image analysis. In order to accomplish this goal, two constraints are imposed on $\boldsymbol{\alpha}$ in (1): 1) ASC ($\sum_{j=1}^p \alpha_j = 1$) and 2) ANC ($\alpha_j \geq 0$ for all $1 \leq j \leq p$). Because there are generally no closed-form solutions to linear mixing problems imposing both constraints, we must rely on numerical algorithms to generate optimal solutions. Fortunately, a fully constrained least squares linear unmixing method recently developed in [27] can be used for this purpose.

III. UFCLSLU

Since data compression generally takes place with no prior knowledge, the FCLSLU must be performed in an unsupervised manner. In this section, we describe an unsupervised FCLSLU method developed in [27] that will generate all necessary target knowledge directly from image data for the linear mixture model used in (1).

A. FCLSLU

In what follows, we will briefly describe the FCLSLU method with details referred to [22], [26], and [27]. First of all, we find the unconstrained optimal least squares estimate of $\boldsymbol{\alpha}$, $\hat{\boldsymbol{\alpha}}_{\text{LS}}$, for

model (1) where both constraints ASC and ANC are not imposed. It can be obtained by

$$\hat{\boldsymbol{\alpha}}_{\text{LS}} = (\mathbf{M}^T \mathbf{M})^{-1} \mathbf{M}^T \mathbf{r} \quad (2)$$

which will be used as an initial estimate of $\boldsymbol{\alpha}$.

Next, the ANC is imposed on model (1), which results in a nonnegatively constrained least squares (NCLS) problem described by

$$\text{Minimize LSE} = (\mathbf{M}\boldsymbol{\alpha} - \mathbf{r})^T (\mathbf{M}\boldsymbol{\alpha} - \mathbf{r}) \text{ subject to } \boldsymbol{\alpha} \geq 0 \quad (3)$$

where the LSE is the least squares error used as the optimal criterion and $\boldsymbol{\alpha} \geq 0$ represents the nonnegativity constraint: $\alpha_j \geq 0$ for all $1 \leq j \leq p$. Since $\boldsymbol{\alpha} \geq 0$ is a set of inequalities, the Lagrange multiplier method is not applicable to finding optimal solutions. In order to resolve this dilemma, we introduce an unknown p -dimensional positive constraint constant vector $\mathbf{c} = [c_1, c_2, \dots, c_p]^T$ with $c_j > 0$ for $1 \leq j \leq p$ to take care of the nonnegativity constraint. By means of \mathbf{c} , we form a Lagrangian J as follows:

$$J = \frac{1}{2} (\mathbf{M}\boldsymbol{\alpha} - \mathbf{r})^T (\mathbf{M}\boldsymbol{\alpha} - \mathbf{r}) + \lambda (\boldsymbol{\alpha} - \mathbf{c}) \quad (4)$$

with $\boldsymbol{\alpha} = \mathbf{c}$ and

$$\left. \frac{\partial J}{\partial \boldsymbol{\alpha}} \right|_{\hat{\boldsymbol{\alpha}}_{\text{NCLS}}} = 0 \Rightarrow \mathbf{M}^T \mathbf{M} \hat{\boldsymbol{\alpha}}_{\text{NCLS}} - \mathbf{M}^T \mathbf{r} + \boldsymbol{\lambda} = 0 \quad (5)$$

which results in the following two iterative equations given by

$$\begin{aligned} \hat{\boldsymbol{\alpha}}_{\text{NCLS}} &= (\mathbf{M}^T \mathbf{M})^{-1} \mathbf{M}^T \mathbf{r} - (\mathbf{M}^T \mathbf{M})^{-1} \boldsymbol{\lambda} \\ &= \hat{\boldsymbol{\alpha}}_{\text{LS}} - (\mathbf{M}^T \mathbf{M})^{-1} \boldsymbol{\lambda} \end{aligned} \quad (6)$$

and

$$\boldsymbol{\lambda} = \mathbf{M}^T (\mathbf{r} - \mathbf{M} \hat{\boldsymbol{\alpha}}_{\text{NCLS}}) \quad (7)$$

which can be used to solve the optimal solution $\hat{\boldsymbol{\alpha}}_{\text{NCLS}}$ and the Lagrange multiplier vector $\boldsymbol{\lambda} = (\lambda_1, \lambda_2, \dots, \lambda_p)^T$.

In order to solve the NCLS problem, an iterative algorithm proposed in [22] is used to generate the solution to (3). It should be noted that the idea of the NCLS algorithm can be traced back to Lawton and Hanson [29]. Two index sets, called a passive set P consisting of all indexes corresponding to positive components in the estimate $\hat{\boldsymbol{\alpha}}_{\text{LS}}$ given by (2) and an active set R containing all indexes corresponding to negative (or zero) components in the estimate $\hat{\boldsymbol{\alpha}}_{\text{LS}}$ are used to iterate (6) and (7). It was shown in [22] and [29] that when an optimal NCLS solution was found, the Lagrange multiplier vector $\boldsymbol{\lambda}$ must satisfy the following equations:

$$\begin{aligned} \lambda_j &= 0, & j \in P \\ \lambda_j &< 0, & j \in R. \end{aligned} \quad (8)$$

An implementation of the NCLS algorithm is provided in the following with more details in [22].

NCLS Algorithm

Step 1): Initialization:

Set the passive set $P^{(0)} = \{1, 2, \dots, p\}$ and active set $R^{(0)} = \emptyset$. Set $k = 0$.

Step 2): Compute $\hat{\boldsymbol{\alpha}}_{\text{LS}}$ using (2). Let $\hat{\boldsymbol{\alpha}}_{\text{NCLS}}^{(k)} = \hat{\boldsymbol{\alpha}}_{\text{LS}}$.

Step 3): At the k th iteration, if all components in $\hat{\alpha}_{\text{NCLS}}^{(k)}$ are positive, the algorithm is terminated. Otherwise, it is continued.

Step 4): Let $k = k + 1$.

Step 5): Move all indexes in $P^{(k-1)}$ that correspond to negative components of $\hat{\alpha}_{\text{NCLS}}^{(k-1)}$ to $R^{(k-1)}$ and the resulting index sets are denoted by $P^{(k)}$ and $R^{(k)}$, respectively. Create a new index set $S^{(k)}$ and set it equal to $R^{(k)}$.

Step 6): Let $\hat{\alpha}_{R^{(k)}}$ denote the vector consisting of all components $\hat{\alpha}_{\text{LS}}$ in $R^{(k)}$.

Step 7): Form a steering matrix $\Phi_{\alpha}^{(k)}$ by deleting all rows and columns in the matrix $(\mathbf{M}^T \mathbf{M})^{-1}$ that are specified by $P^{(k)}$.

Step 8): Calculate $\lambda^{(k)} = (\Phi_{\alpha}^{(k)})^{-1} \hat{\alpha}_{R^{(k)}}$. If all components in $\lambda^{(k)}$ are negative, go to Step 13). Otherwise, continue.

Step 9): Calculate $\lambda_{\max}^{(k)} = \arg\{\max_j \lambda_j^{(k)}\}$ and move the index in $R^{(k)}$ that corresponds to $\lambda_{\max}^{(k)}$ to $P^{(k)}$.

Step 10): Form another matrix $\Psi_{\lambda}^{(k)}$ by deleting every column of $(\mathbf{M}^T \mathbf{M})^{-1}$ specified by $P^{(k)}$.

Step 11): Set $\hat{\alpha}_{S^{(k)}} = \hat{\alpha}_{\text{LS}} - \Psi_{\lambda}^{(k)} \lambda^{(k)}$.

Step 12): If any components of $\hat{\alpha}_{S^{(k)}}$ in $S^{(k)}$ are negative, then move these components from $P^{(k)}$ to $R^{(k)}$. Go to Step 6).

Step 13): Form another matrix $\Psi_{\lambda}^{(k)}$ by deleting every column of $(\mathbf{M}^T \mathbf{M})^{-1}$ specified by $P^{(k)}$.

Step 14): Set $\hat{\alpha}_{\text{NCLS}}^{(k)} = \hat{\alpha}_{\text{LS}} - \Psi_{\lambda}^{(k)} \lambda^{(k)}$. Go to Step 3).

In order to satisfy the second constraint ASC, we include the ASC in the signature matrix \mathbf{M} by introducing a new signature matrix \mathbf{N} , defined by

$$\mathbf{N} = \begin{bmatrix} \delta \mathbf{M} \\ \mathbf{1}^T \end{bmatrix} \quad (9)$$

with $\mathbf{1}^T = (\underbrace{1 \ 1 \ \dots \ 1}_p)$, and a vector \mathbf{s} denoted by

$$\mathbf{s} = \begin{bmatrix} \delta \mathbf{r} \\ 1 \end{bmatrix}. \quad (10)$$

The introduction of the parameter δ in (9) and (10) is to control the impact of the ASC. Using these two equations, an FCLSLU algorithm can be derived directly from the NCLS algorithm by replacing \mathbf{M} and \mathbf{r} used in the NCLS algorithm with \mathbf{N} and \mathbf{s} .

B. UFCLSLU

The FCLSLU requires a complete knowledge of the target signature matrix \mathbf{M} . In order for it to be applied to a situation where no *a priori* information is available, an unsupervised process is needed to generate from the data the desired target information for the FCLSLU. Two criteria were previously developed for this purpose. One was the nearest neighbor rule from which an unsupervised vector quantization method was derived to find interferers [30]. The other is the target generation process proposed in [31], which was based on the principle of orthogonality. Instead, this paper will use the least squares

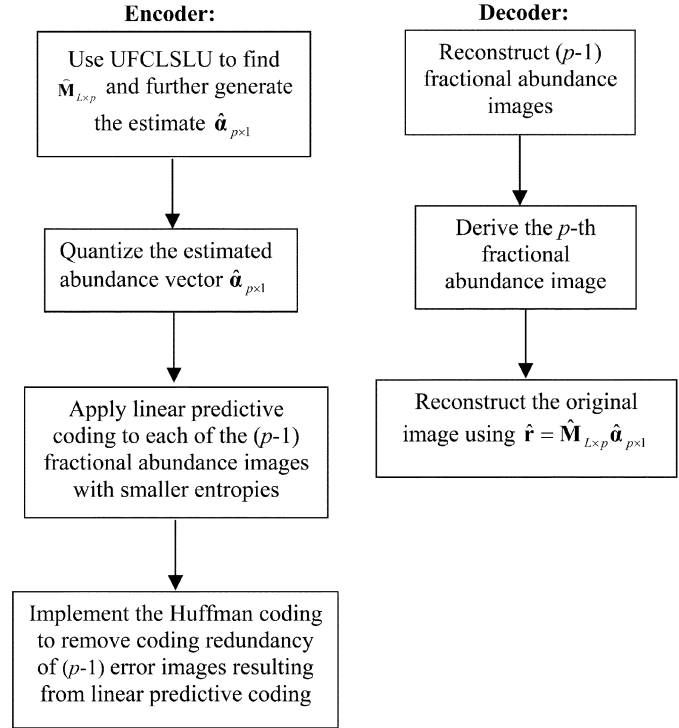


Fig. 1. Block diagram of UFCLSLU-based compression algorithm.

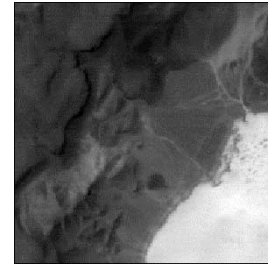


Fig. 2. AVIRIS LCVF scene of size 200×200 (band 100).

TABLE I
SNR, PSNR, AND CR PRODUCED BY THE PCA, LSLU, FCLSLU, AND UFCLSLU METHODS FOR THE AVIRIS EXPERIMENTS

	PCA	LSLU	FCLSLU	UFCLSLU
SNR(dB)	30.55	35.00	33.31	33.79
PSNR(dB)	36.56	41.00	39.32	39.80
CR	57.12:1	69.84:1	114.17:1	89.83:1

error (LSE)-based criterion proposed in [27] as an alternative. Its idea can be described as follows.

Initially, we can select any arbitrary pixel vector as an initial desired target denoted by \mathbf{t}_0 . However, a good choice, but not necessarily the best choice, may be a pixel vector with the maximum length, which has the highest intensity, i.e., the brightest pixel in the image scene. In any case, our experiments found that the brightest pixel was always extracted later on, if it was not used as an initial target pixel in the first place. We then assume that all other pixel vectors in the image scene are pure pixels made up of \mathbf{t}_0 with 100% abundance. Of course, this is generally not true. So, we find a pixel vector that has the largest LSE between itself and \mathbf{t}_0 , and we select it as a first target pixel vector denoted by \mathbf{t}_1 . Because the LSE between \mathbf{t}_0 and \mathbf{t}_1 is the

TABLE II
VARIANCES OF FRACTIONAL ABUNDANCE IMAGES USING UNCONSTRAINED AND CONSTRAINED LEAST SQUARES ESTIMATION

	cinder	playa	rhyolite	vegetation	shade
LSLU	0.0261	0.1056	0.0273	0.0192	0.0917
FCLSLU	0.0159	0.0975	0.0128	0.0165	0.0750
UFCLSLU	0.0176	0.0729	0.0122	0.0110	0.0451

largest, it can be expected that \mathbf{t}_1 is most distinct from \mathbf{t}_0 . We then form a target signature matrix $\mathbf{M} = [\mathbf{t}_0 \ \mathbf{t}_1]$ and create the matrix \mathbf{N} and \mathbf{s} using (9) and (10). The FCLSLU algorithm is then used to estimate the abundance fractions for \mathbf{t}_0 and \mathbf{t}_1 , denoted by $\hat{\alpha}_0^{(1)}(\mathbf{r})$ and $\hat{\alpha}_1^{(1)}(\mathbf{r})$ for each pixel \mathbf{r} , respectively. Here, \mathbf{r} is included in the estimated abundance fractions $\hat{\alpha}_0^{(1)}(\mathbf{r})$ and $\hat{\alpha}_1^{(1)}(\mathbf{r})$ to emphasize that $\hat{\alpha}_0^{(1)}(\mathbf{r})$ and $\hat{\alpha}_1^{(1)}(\mathbf{r})$ are functions of \mathbf{r} and vary with \mathbf{r} . The superscript indicates the number of iterations currently being executed. Now, we find an optimal constrained linear mixture of \mathbf{t}_0 and \mathbf{t}_1 , $\hat{\alpha}_0^{(1)}(\mathbf{r})\mathbf{t}_0 + \hat{\alpha}_1^{(1)}(\mathbf{r})\mathbf{t}_1$, to approximate the \mathbf{r} . We then calculate the LSE between \mathbf{r} and its estimated linear mixture $\hat{\alpha}_0^{(1)}(\mathbf{r})\mathbf{t}_0 + \hat{\alpha}_1^{(1)}(\mathbf{r})\mathbf{t}_1$ for all image pixel vectors \mathbf{r} . Once again, a pixel vector that yields the largest LSE between itself and its estimated linear mixture will be selected to be a second target pixel vector \mathbf{t}_2 . As expected, such a selected target pixel has the largest projection orthogonal to the space linearly spanned by \mathbf{t}_0 and \mathbf{t}_1 . In other words, the pixel that yields the largest LSE resulting from a constrained linear mixture approximation is a most likely target pixel vector yet to be found in the image scene. The same procedure of using the FCLSLU algorithm with $\mathbf{M} = [\mathbf{t}_0 \ \mathbf{t}_1 \ \mathbf{t}_2]$ is repeated until the resulting LSE is below a prescribed error threshold. It should be noted that if there is partial knowledge available *a priori*, it can be incorporated into the above process. For example, if more than one target signature is known, we can select those target signatures as an initial target set and then follow the procedure described above until the LSE is sufficiently small. The procedure outlined as above is called unsupervised FCLSLU algorithm, which can be summarized as follows.

UFCLSLU Algorithm

Step 1): Initial condition:
Select ε to be a prescribed error threshold,
and let $\mathbf{t}_0 = \arg\{\max_{\mathbf{r}}[\mathbf{r}^T \mathbf{r}]\}$ where \mathbf{r} is run over all image pixel vectors. Let $k = 0$.
Step 2): Find \mathbf{t}_1 that yields the largest $\text{LSE}^{(0)}(\mathbf{r}) = (\mathbf{r} - \mathbf{t}_0)^T(\mathbf{r} - \mathbf{t}_0)$, i.e., $\mathbf{t}_1 = \arg\{\max_{\mathbf{r}} \text{LSE}^{(0)}(\mathbf{r})\}$.
Step 3): Let $k \leftarrow k + 1$, and apply the FCLSLU algorithm with the signature matrix $\mathbf{M} = [\mathbf{t}_0, \mathbf{t}_1, \dots, \mathbf{t}_k]$, $\mathbf{N} = \begin{bmatrix} \delta \mathbf{M} \\ \mathbf{1}^T \end{bmatrix}$, and $\mathbf{s} = \begin{bmatrix} \delta \mathbf{r} \\ \mathbf{1} \end{bmatrix}$ to estimate the abundance fractions of $\mathbf{t}_0, \mathbf{t}_1, \dots, \mathbf{t}_k$, $\hat{\alpha}_0^{(k)}(\mathbf{r}), \hat{\alpha}_1^{(k)}(\mathbf{r}), \dots, \hat{\alpha}_{k-1}^{(k)}(\mathbf{r})$.
Step 4): Find the least squares error defined by

$$\text{LSE}^{(k)}(\mathbf{r}) = \left(\mathbf{r} - \left[\sum_{i=0}^k \hat{\alpha}_i^{(k)}(\mathbf{r}) \mathbf{t}_i \right] \right)^T \left(\mathbf{r} - \left[\sum_{i=0}^k \hat{\alpha}_i^{(k)}(\mathbf{r}) \mathbf{t}_i \right] \right) \quad (11)$$

TABLE III
SNR, PSNR, AND CR PRODUCED BY THE PCA, LSLU, FCLSLU, AND UFCLSLU METHODS WITH DIFFERENT ROUND-OFF ERRORS FOR THE HYDICE EXPERIMENTS

	5×10^{-2}	5×10^{-3}	5×10^{-4}
SNR(dB)	22.32	33.79	34.38
PSNR(dB)	28.33	39.80	40.39
CR	239.82:1	89.83:1	49.47:1

and check the error if $\text{LSE}^{(k)}(\mathbf{r}) < \varepsilon$ for all \mathbf{r} . If it is, the algorithm stops. Otherwise, continue.

Step 5): Find $\mathbf{t}_{k+1} = \arg\{\max_{\mathbf{r}} \text{LSE}^{(k)}(\mathbf{r})\}$. Go to Step 3).

It should be noted that $\{\text{LSE}^{(k)}(\mathbf{r})\}$ is a monotonically decreasing sequence at k ; thus it converges. The computational complexity of the UFCLSLU algorithm can be estimated based on the number of computations performed. The major computation in each iteration comes from the calculation of the inverse of the steering matrix \mathbf{N} . It increases with p^3 as the algorithm is applied to each pixel vector, where p is the number of target signatures used to calculate the LSE, and \mathbf{N} is a $p \times p$ matrix. Therefore, the total number of computations is on the order of $n \times p^3$, where n is the total number of pixel vectors in the image scene.

IV. UFCLSLU-BASED HYPERSPECTRAL IMAGE COMPRESSION

Over the past years, criteria to measure effectiveness of lossless or lossy compression have been focused on the fidelity of image quality such as SNR, entropy, MSE, etc., rather than applications. In this section, we describe how we can take advantage of applications to achieve high compression ratios while preserving desired information. As indicated in the introduction, hyperspectral sensors can uncover many unknown signal sources that cannot be identified by visually or *a priori*. These unknown or unidentified signatures may include natural background signatures and unwanted clutters/interferers that may hinder image interpretation. Under such circumstances, lossless compression seems to offer no advantage for image analysis because it also preserves such unknown and unwanted information such as noise and interference. On the other hand, lossy compression only preserves information in some optimal sense of entropy or MSE. However, in military and intelligence applications, targets of interest are generally man-made and relatively small, such as vehicles. They usually occur with low probabilities and account for a small population, but are crucial to image analysis. Such information may be very likely to be sacrificed by lossy compression unless these targets are taken into account during data compression. This is particularly important for the HYDICE sensor, which can extract very

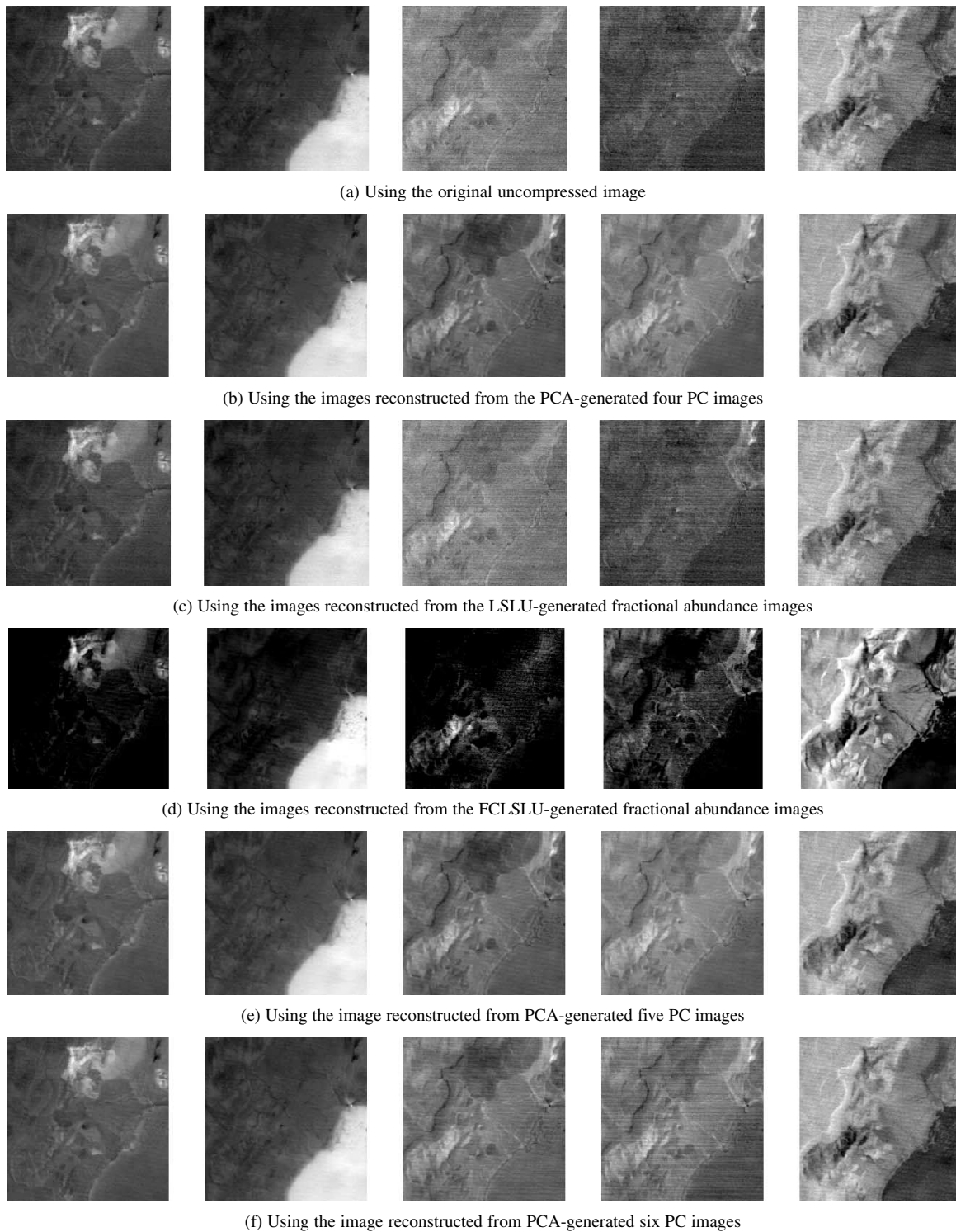


Fig. 3. (a) Supervised classification results produced by the original uncompressed image for the AVIRIS experiment. (b) Supervised classification results produced by the images reconstructed from the four principal component images for the AVIRIS experiment. (c) Supervised classification results produced by the images reconstructed from the LSLU-generated fractional abundance images for the AVIRIS experiment. (d) Supervised classification results produced by the images reconstructed from the FCLSLU-generated fractional abundance images for the AVIRIS experiment. (e) Supervised classification results produced by the images reconstructed from the five principal component images for the AVIRIS experiment. (f) Supervised classification results produced by the images reconstructed from the six principal component images for the AVIRIS experiment.

small targets with size ranging from 1–4 m with flight attitudes from 5000–15 000 ft. Such small targets generally occupy only a few pixels. Compared to the entire image scene, these targets can be easily overlooked and compromised by lossy compression. Furthermore, strong interferers, such as those resulting

from scratches, may dominate small targets, and their existence will be considered to be important information from an image quality point of view. So, these interferers will be very likely retained in the compressed image. As an example, when PCA is performed, small targets may appear in minor components,

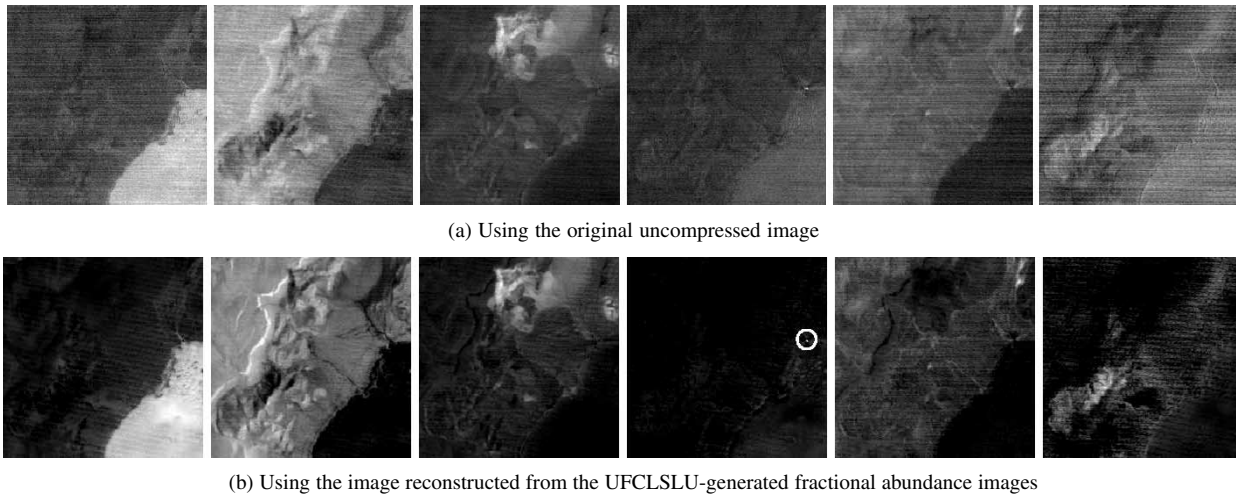


Fig. 4. (a) Unsupervised classification results produced by the original uncompressed image for the AVIRIS experiment. (b) Unsupervised classification results produced by the images reconstructed from the images reconstructed from the UFCLSLU-generated fractional abundance images for the AVIRIS experiment.

while strong interferers may show up in the first few principal components, which may confuse image analysis. In order to cope with this problem, application-based lossy compression is a more realistic approach. In this section, we consider an approach to target detection and classification-based compression. As will be shown in the following experiments, it not only can achieve very high compression ratios, but can also improve performance of image analysis in some cases.

A. UFCLSLU-Based Compression

The idea of the UFCLSLU is to represent a hyperspectral image cube by a set of fractional abundance images. More precisely, for each pixel vector \mathbf{r} of L dimensions, its associated abundance vector $\boldsymbol{\alpha}$ of p dimensions is used as a fingerprint of the \mathbf{r} with respect to p target signatures $\mathbf{t}_1, \mathbf{t}_2, \dots, \mathbf{t}_p$ used in model (1). Since no prior knowledge is available, these p target signatures must be obtained directly from the image data by an unsupervised means. In order for $\boldsymbol{\alpha}$ to faithfully represent \mathbf{r} , $\boldsymbol{\alpha}$ must satisfy constraints ASC and ANC. In this case, the UFCLSLU algorithm described in Section III can be used to generate an appropriate set of target signatures for model (1). The implementation of an UFCLSLU-based compression algorithm can be described as follows.

UFCLSLU-based Compression Algorithm

Step 1): Use the UFCLSLU algorithm in Section III to generate a set of targets of interest, denoted by $\{\hat{\mathbf{t}}_1, \hat{\mathbf{t}}_2, \dots, \hat{\mathbf{t}}_p\}$ to form an estimated target signature matrix, denoted by $\hat{\mathbf{M}} = [\hat{\mathbf{t}}_1, \hat{\mathbf{t}}_2, \dots, \hat{\mathbf{t}}_p]$ where $\hat{\mathbf{t}}_j = (\hat{t}_{j1}, \hat{t}_{j2}, \dots, \hat{t}_{jL})^T$ for $1 \leq j \leq p$.

Step 2): For the i th image pixel vector $\mathbf{r}_i = (r_{i1}, r_{i2}, \dots, r_{iL})^T$, use the FCLSLU algorithm to estimate the corresponding target abundance fractions, denoted by $\{\hat{\alpha}_1(\mathbf{r}_i), \hat{\alpha}_2(\mathbf{r}_i), \dots, \hat{\alpha}_p(\mathbf{r}_i)\}$ and estimate $\hat{\mathbf{r}}_i$ by

$$\hat{\mathbf{r}}_i = \hat{\mathbf{M}}\hat{\boldsymbol{\alpha}}(\mathbf{r}_i) \quad (12)$$

where $\hat{\mathbf{r}}_i = (\hat{r}_{i1}, \hat{r}_{i2}, \dots, \hat{r}_{iL})^T$ and $\hat{r}_{il} = \sum_{j=1}^p t_{jl}\hat{\alpha}_j(\mathbf{r}_i)$. Note that (12) is a reconstruction of \mathbf{r}_i from the p FCLSLU-generated fractional abundance images, and the noise term in (1) has been absorbed in (12) as an estimation error.

Step 3): Construct p fractional abundance images $\{\hat{\alpha}_1(\mathbf{r}_i), \hat{\alpha}_2(\mathbf{r}_i), \dots, \hat{\alpha}_p(\mathbf{r}_i)\}$ for all pixel vectors \mathbf{r}_i in the image.

Step 4): Apply lossless predictive coding to further reduce spatial redundancy within each of the p fractional abundance images.

Step 5): Use Huffman coding to encode the predictive errors resulting from Step 4).

Fig. 1 depicts a diagram of the UFCLSLU-based compression algorithm. Five comments related to the UFCLSLU are noteworthy.

- Due to the fact that there is no prior knowledge available for an image to be compressed, the UFCLSLU is generally required.
- Since $\{\hat{\alpha}_1(\mathbf{r}_i), \hat{\alpha}_2(\mathbf{r}_i), \dots, \hat{\alpha}_p(\mathbf{r}_i)\}$ satisfies the ASC, only $p - 1$ fractional abundance images of smallest entropies are needed for encoding for each pixel vector \mathbf{r}_i in Step 3). In other words, the only fractional abundance image that is not required to encode is the one with maximum entropy.
- The compression ratio is determined by the number of target signatures resident in the image scene, i.e., p , not the data dimensionality L . The smaller p is, the higher the compression ratio is.
- The UFCLSLU-based compression algorithm can also be implemented as unconstrained or nonnegatively constrained versions with the fully constrained abundance vector $\hat{\boldsymbol{\alpha}}(\mathbf{r}_i)$ replaced by $\hat{\boldsymbol{\alpha}}_{\text{LS}}(\mathbf{r}_i)$ given by (2) or $\hat{\boldsymbol{\alpha}}_{\text{NCLS}}(\mathbf{r}_i)$ generated by the NCLS algorithm. But in these cases, all the p abundance fractions $\{\hat{\alpha}_1(\mathbf{r}_i), \hat{\alpha}_2(\mathbf{r}_i), \dots, \hat{\alpha}_p(\mathbf{r}_i)\}$ must be encoded in Step 3). It should be further noted that when the UFCLSLU-based compression algorithm is implemented as

an unconstrained LSMA, it is reduced to the approach in [19]. Comparing (12) to model (1), there is no noise term \mathbf{n} in (12). This is because (12) is a lossy reconstruction, where the \mathbf{n} has been absorbed by the estimation error resulting from lossy decompression.

- As noted, our proposed compression technique is a method that compresses spectral redundancy pixel-by-pixel. It uses the UFCLSLU algorithm to compress image data to generate a set of p fractional abundance images that show abundance fractions of targets of interest present in the image data. As a result of such LSMA compression, the image background is significantly compressed, where the interpixel spatial correlation is also substantially reduced. Therefore, the remaining redundancy of interest is the coding redundancy produced by target pixels present in the UFCLSLU-generated fractional abundance images. In this case, a simple entropy coding scheme such as Huffman coding may perform well without appealing for a sophisticated coding technique. Applying lossless coding to the UFCLSLU-generated fractional abundance images can show how much spectral compression error alone can be from our proposed technique. Of course, more compression can be achieved by lossy spatial coding. However, since the abundance fraction of each pixel after the UFCLSLU spectral compression is crucial, preserving such information is very important for future data decompression. Therefore, lossy spatial compression may not be appropriate, since it may result in loss of target information that will be significant for data decompression.

B. Practical Implementation Issues of UFCLSLU-Based Compression

Some practical issues in implementing the UFCLSLU need to be addressed in this section. Since the abundance fractions generated by the UFCLSLU are real values within the range of $[0, 1]$, a simplest encoding scheme is to multiply their values by 10^b with $b \geq 1$ and round off their resulting values to integral values that will be encoded. For example, if 10^b is multiplied, then the precision is 10^{-b} and the round-off error for precision of 10^{-b} is $5 \times 10^{-(b+1)}$. The higher the precision, the lower the compression ratio. According to our experiments, a very high compression ratio can be achieved by precision of 10^{-1} with the round-off error 5×10^{-2} . In this case, the number of values required for Huffman coding is less than or equal to ten. So the corresponding compression ratio is high, but the resulting SNR is relatively low. On the other hand, when the precision is increased to 10^{-3} with the round-off error 5×10^{-4} , the resulting SNR is improved, but the improvement may not be significant. However, the compression ratio obtained is considerably reduced. Since the values of these abundance fractions are constrained to the range of $[0, 1]$, a good compromise is precision of 10^{-2} with the round-off error 5×10^{-3} . The round-off error described above is the major compression error incurred in the UFCLSLU-based compression algorithm in addition to the model error introduced by (1). If the signatures used in the linear mixture model specified by (1) well represent the image scene, the model error will be small. The error resulting from

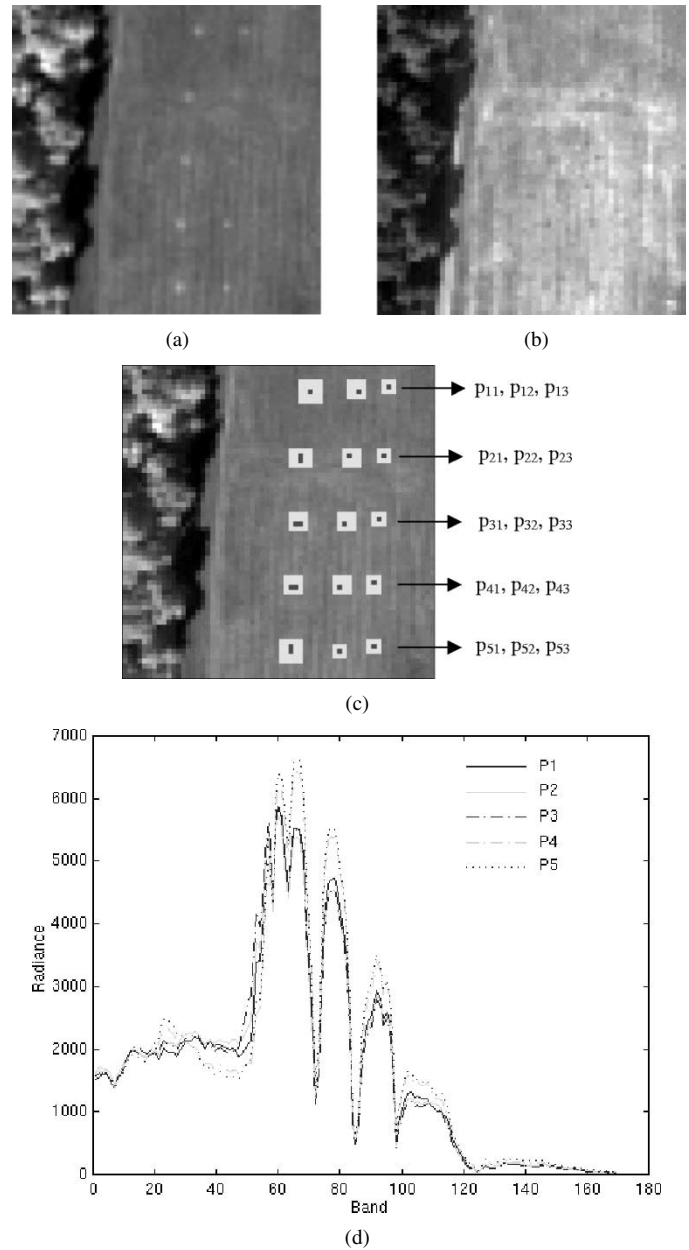


Fig. 5. (a) HYDICE scene of band 10 (64×64). (b) A HYDICE scene of band 30 (64×64). (c) Spatial locations of 15 panels provided by ground truth. (d) Spectra of P1, P2, P3, P4, and P5.

the UFCLSLU will be very small, if the error threshold ϵ used in the UFCLSLU algorithm is set to a small value.

V. EXPERIMENTAL RESULTS

In this section, we conduct a series of experiments to evaluate the proposed UFCLSLU-based compression technique using two sets of real hyperspectral image data, AVIRIS and HYDICE images. Three common error criteria, referred to as SNR, PSNR, and compression ratio (CR), are also used for performance evaluation and defined as follows:

$$\text{SNR} = 10 \log_{10} \left[\frac{\sum_i \mathbf{r}_i^T \mathbf{r}_i}{\sum_i (\mathbf{r}_i - \hat{\mathbf{r}}_i)^T (\mathbf{r}_i - \hat{\mathbf{r}}_i)^T} \right] \quad (13)$$

TABLE IV
SNR, PSNR, AND CR PRODUCED BY THE UFCLSLU METHODS WITH DIFFERENT ROUND-OFF ERRORS FOR HYDICE EXPERIMENTS

	PCA	LSLU	FCLSLU	UFCLSLU (5 target signatures)	UFCLSLU (35 target signatures)
SNR(dB)	22.34	25.48	22.10	27.72	38.05
PSNR(dB)	27.56	30.69	25.56	32.94	43.27
CR	22.39:1	48.99:1	121.49:1	138.01:1	37.63:1

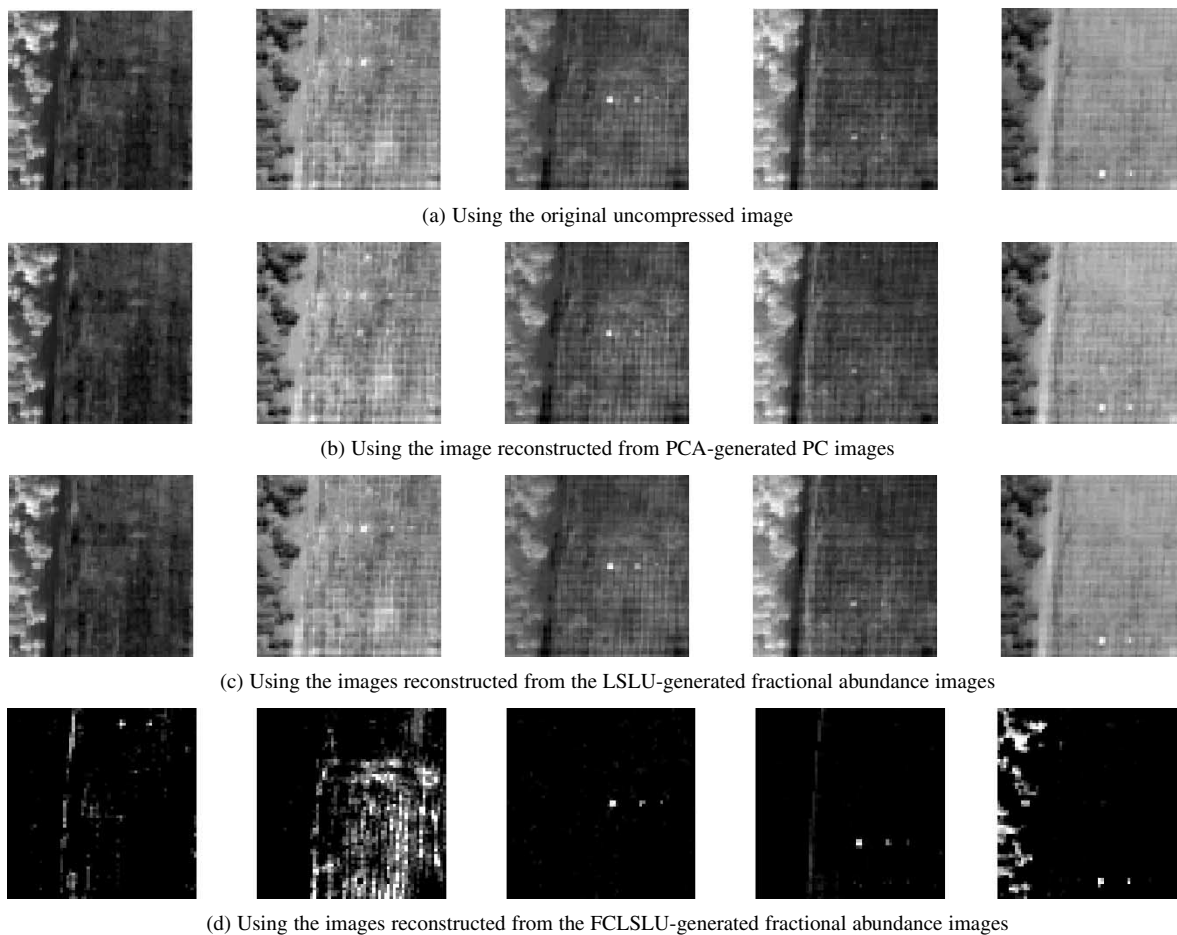


Fig. 6. (a) Supervised classification results produced by the original uncompressed image for the HYDICE experiment. (b) Supervised classification results produced by the images reconstructed from the principal component images for the HYDICE experiment. (c) Supervised classification results produced by the images reconstructed from the LSLU-generated fractional abundance images for the HYDICE experiment. (d) Supervised classification results produced by the images reconstructed from the FCLSLU-generated fractional abundance images for the HYDICE experiment.

$$\text{PSNR} = 10 \log_{10} \left[\frac{\max_i \{\mathbf{r}_i^T \mathbf{r}_i\}}{\frac{1}{n} \sum_i (\mathbf{r}_i - \hat{\mathbf{r}}_i)^T (\mathbf{r}_i - \hat{\mathbf{r}}_i)^T} \right] \quad (14)$$

$$\text{CR} = \frac{\text{original image file size}}{\text{compressed image file size}} \quad (15)$$

CR defined by (15) is based on image file size rather than bit rate and is adopted for the following reason. For example, an AVIRIS image of size 200×200 contains a total of 200×200 data vectors, and each of these data vectors is made up of 224 data points. In the AVIRIS scene to be studied in our experiments, the range of pixel values is from 1800–0. So, 11 bits are needed to represent each data point in binary expansion, and the total bits required are $200 \times 200 \times 224 \times 11 = 98\,560\,000$ bits. After the water bands and low SNR bands are removed, 158 bands remained. This reduces the total number of bits to $200 \times 200 \times 158 \times 11 = 69\,520\,000$ bits. If it is

compressed by either the FCLSLU or UFCLSLU, only $p - 1$ fractional abundance images are required for decompression, in which case the total number of data points required for coding is reduced to $200 \times 200 \times (p - 1)$. Similarly, for the HYDICE scene of size 64×64 that was studied in our experiments, the range of abundance values is between 10000 and -6 , where the negative abundance values may be resulting from either bad pixels or gains offset by correction. So, 15 bits are required for each data point, and the total required bits are $64 \times 64 \times 210 \times 15 = 12\,902\,400$. After the water bands and low SNR bands are removed, 169 bands are still retained. In this case, the total bits required for the image file are reduced to $64 \times 64 \times 169 \times 15 = 10\,383\,360$.

A. AVIRIS Data Experiments

The AVIRIS image used in the following experiments is shown in Fig. 2(a). It is the same data considered in [20] that

TABLE V

(a) TALLY OF THE NUMBER OF PANEL PIXELS DETECTED IN FIG. 6(a). (b) TALLY OF THE NUMBER OF PANEL PIXELS DETECTED IN FIG. 6(b). (c) TALLY OF THE NUMBER OF PANEL PIXELS DETECTED IN FIG. 6(c). (d) TALLY OF THE NUMBER OF PANEL PIXELS DETECTED IN FIG. 6(d)

	N _P	$\alpha = 0.1$		$\alpha = 0.2$		$\alpha = 0.3$		$\alpha = 0.4$		$\alpha = 0.5$		$\alpha = 0.6$		$\alpha = 0.7$		$\alpha = 0.8$		$\alpha = 0.9$	
		N _D	N _F																
P1	3	3	3934	3	2775	3	1126	0	523	0	341	0	203	0	81	0	22	0	6
P2	4	4	4025	4	3970	4	3832	4	3578	4	2676	4	1167	4	217	3	40	2	2
P3	4	4	4029	4	3903	4	2668	4	948	4	202	3	34	2	0	2	0	1	0
P4	4	4	4034	4	3534	4	1884	3	998	3	700	3	458	0	213	0	77	0	0
P5	4	4	4018	4	3917	4	3686	4	3411	4	2964	4	1399	3	54	3	2	2	0
Total	19	19	20040	19	18099	19	13196	15	9458	15	6883	14	3261	9	565	8	141	5	8

(a)

	N _P	$\alpha = 0.1$		$\alpha = 0.2$		$\alpha = 0.3$		$\alpha = 0.4$		$\alpha = 0.5$		$\alpha = 0.6$		$\alpha = 0.7$		$\alpha = 0.8$		$\alpha = 0.9$	
		N _D	N _F																
P1	3	3	3926	3	2805	2	1162	0	532	0	348	0	211	0	91	0	26	0	6
P2	4	4	4021	4	3974	4	3856	4	3679	4	3102	4	1732	4	573	2	101	0	14
P3	4	4	4025	4	3907	4	2901	4	1336	4	402	3	105	2	16	2	0	1	0
P4	4	4	4036	4	3746	4	2137	3	1060	3	730	0	485	0	250	0	89	0	22
P5	4	4	4029	4	3955	4	3779	4	3527	4	3270	4	2573	4	760	3	35	2	2
Total	19	19	20037	19	18387	18	13835	15	10134	15	7852	11	5106	10	1690	7	251	3	44

(b)

	N _P	$\alpha = 0.1$		$\alpha = 0.2$		$\alpha = 0.3$		$\alpha = 0.4$		$\alpha = 0.5$		$\alpha = 0.6$		$\alpha = 0.7$		$\alpha = 0.8$		$\alpha = 0.9$	
		N _D	N _F																
P1	3	3	3935	3	2785	3	1132	0	523	0	341	0	203	0	81	0	22	0	6
P2	4	4	4025	4	3969	4	3833	4	3580	4	2689	4	1185	4	220	3	41	2	2
P3	4	4	4028	4	3896	4	2627	4	942	4	200	3	33	2	0	2	0	1	0
P4	4	4	4034	4	3525	4	1894	3	996	3	703	3	455	0	212	0	77	0	16
P5	4	4	4020	4	3917	4	3687	4	3417	4	2970	4	1407	3	54	3	2	2	0
Total	19	19	20042	19	18092	19	13173	15	9458	15	6903	14	3285	9	567	5	142	2	24

(c)

	N _P	$\alpha = 0.1$		$\alpha = 0.2$		$\alpha = 0.3$		$\alpha = 0.4$		$\alpha = 0.5$		$\alpha = 0.6$		$\alpha = 0.7$		$\alpha = 0.8$		$\alpha = 0.9$	
		N _D	N _F																
P1	3	2	857	2	626	2	445	2	298	2	200	2	109	1	60	1	23	1	6
P2	4	4	1274	4	1011	4	762	3	553	3	349	1	224	1	135	0	98	0	90
P3	4	4	13	4	3	4	3	4	2	3	1	3	0	2	0	2	0	1	0
P4	4	3	159	2	25	1	2	1	0	1	0	1	0	1	0	1	0	1	0
P5	4	4	718	3	610	3	508	3	414	3	338	3	266	3	185	3	117	3	75
Total	19	17	3021	16	2275	15	1720	14	1267	13	888	10	599	8	380	7	238	6	171

(d)

have been studied extensively in the literature. Atmospheric water bands and low SNR bands have been removed from the image data. As a result, only 158 bands are used for compression. The image scene in Fig. 2(a) is a subscene of 200×200 pixels extracted directly from the upper left corner of the Lunar Crater Volcanic Field (LCVF) in Northern Nye County, NV, shown in Fig. 2(b). According to the ground truth knowledge, there are five different materials of interest present in this image scene: "red oxidized basaltic cinders," "rhyolite," "playa (dry lakebed)," "shade," and "vegetation." As noted in [19], a least squares unconstrained orthogonal projection-based compression was proposed to compress the same AVIRIS scene in Fig. 2(a). Four compression methods were used for comparative analysis, which are the PCA-based compression, the supervised OSP method in [19] referred to as least squares linear unmixing (LSLU), supervised FCLSLU-based compression, and our proposed UFCLSLU method. The reason PCA-based compression was included

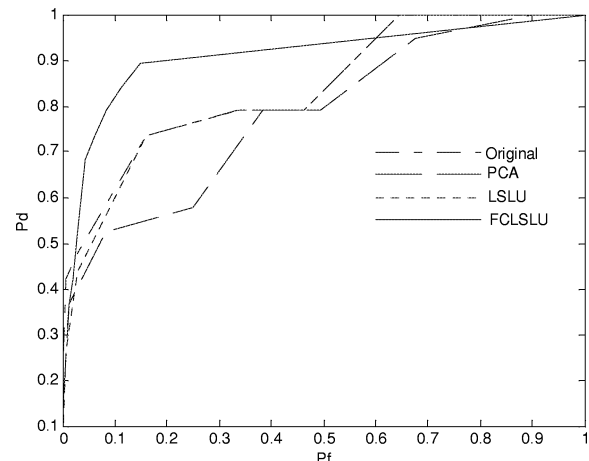


Fig. 7. ROC curves for the overall panel detection performance in Fig. 6.

is that it is a typical transformed coding that transforms the original image data into separate principal components (PCs).

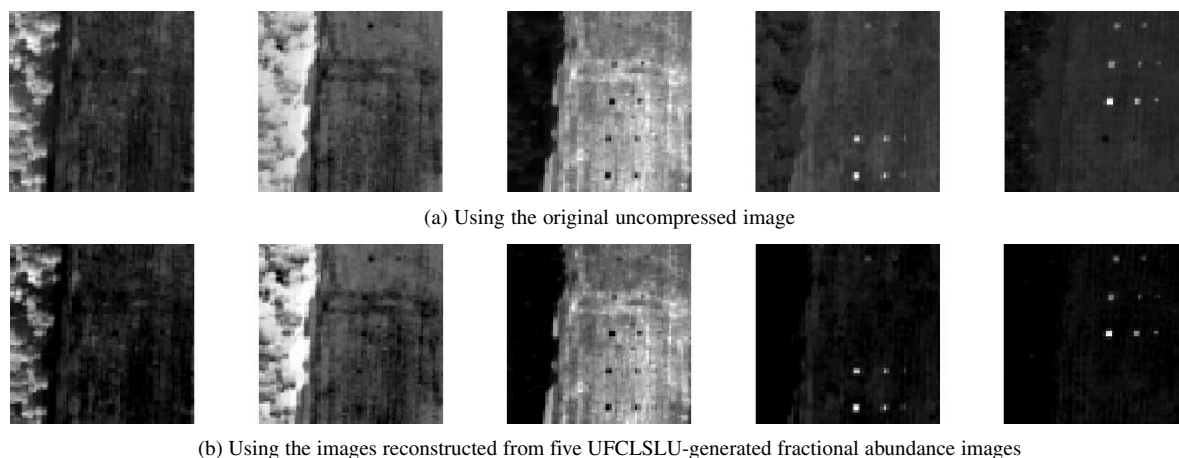


Fig. 8. (a) Unsupervised classification results produced by the original uncompressed image for the HYDICE experiment. (b) Unsupervised classification results produced by the images reconstructed from five UFCLSLU-generated fractional abundance images for the HYDICE experiment.

TABLE VI
(a) TALLY OF THE NUMBER OF PANEL PIXELS DETECTED IN FIG. 8(a). (b) TALLY OF THE NUMBER OF PANEL PIXELS DETECTED IN FIG. 8(b)

	N _P	α = 0.1			α = 0.2		α = 0.3		α = 0.4		α = 0.5		α = 0.6		α = 0.7		α = 0.8		α = 0.9	
		N _D	N _F																	
P1	3	2	70	2	16	1	13	1	9	0	6	0	5	0	4	0	4	0	2	
P2	4	4	67	4	14	3	9	2	7	0	6	0	5	0	4	0	4	0	2	
P3	4	4	65	4	12	4	6	3	5	3	0	2	0	2	0	2	0	2	0	
P4	4	4	721	4	32	3	7	3	7	3	5	3	4	2	3	1	2	0	1	
P5	4	4	724	4	30	3	7	3	6	3	3	3	3	2	2	1	1	0	0	
Total	19	18	1647	18	104	14	42	12	34	9	20	8	17	7	13	5	11	3	5	

(a)

	N _P	α = 0.1			α = 0.2		α = 0.3		α = 0.4		α = 0.5		α = 0.6		α = 0.7		α = 0.8		α = 0.9	
		N _D	N _F																	
P1	3	2	33	2	16	1	13	1	9	0	6	0	4	0	4	0	4	0	2	
P2	4	4	29	4	13	3	9	2	7	0	6	0	4	0	4	0	4	0	2	
P3	4	4	27	4	11	4	6	3	4	3	0	2	0	2	0	2	0	2	0	
P4	4	4	657	4	26	3	7	3	7	3	5	3	4	2	3	1	2	0	1	
P5	4	4	658	4	24	3	7	3	6	3	4	3	3	2	2	1	1	0	0	
Total	19	18	1404	18	90	14	42	12	33	9	21	8	15	7	13	5	11	3	5	

(b)

In the AVIRIS experiment, the first four PC images were retained because they included 99.88% energy, and there is no visible information present in PC images afterward. When the LSLU and the supervised FCLSLU were applied, the five signatures “cinders, rhyolite, playa, shade, vegetation” were used as the prior target knowledge. Since the UFCLSLU-based compression is unsupervised and no prior target knowledge was needed, the UFCLSLU generated target signatures by its own. As a result, six signatures were extracted from the data by the UFCLSLU, which included five signatures used in the supervised LSLU and FCLSLU plus an additional signature, an anomaly detected in [22] marked by a white circle in Fig. 4. The approach implemented in the spatial coding of the PC images and the fractional abundance images was a third-order linear predictive coding method that used the three previous pixels in the same row, followed by the Huffman coding. The order of three is an empirical choice, which provides the best trade-off between CR and computing time in our experiments. In general, applying linear predictive coding only brings about a 10% improvement in the CRs, compared to that produced

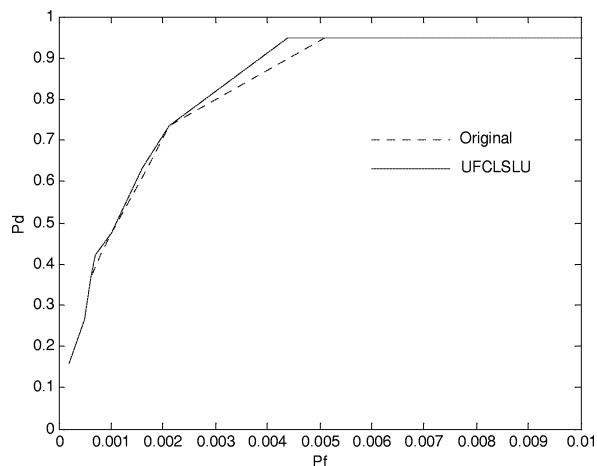


Fig. 9. ROC curves for the overall panel detection performance in Fig. 8.

without it. The pixel values in the PC images and the fractional abundance images were rounded off with an error tolerance of 5×10^{-3} . Table I tabulates SNRs, PSNRs, and CRs of these

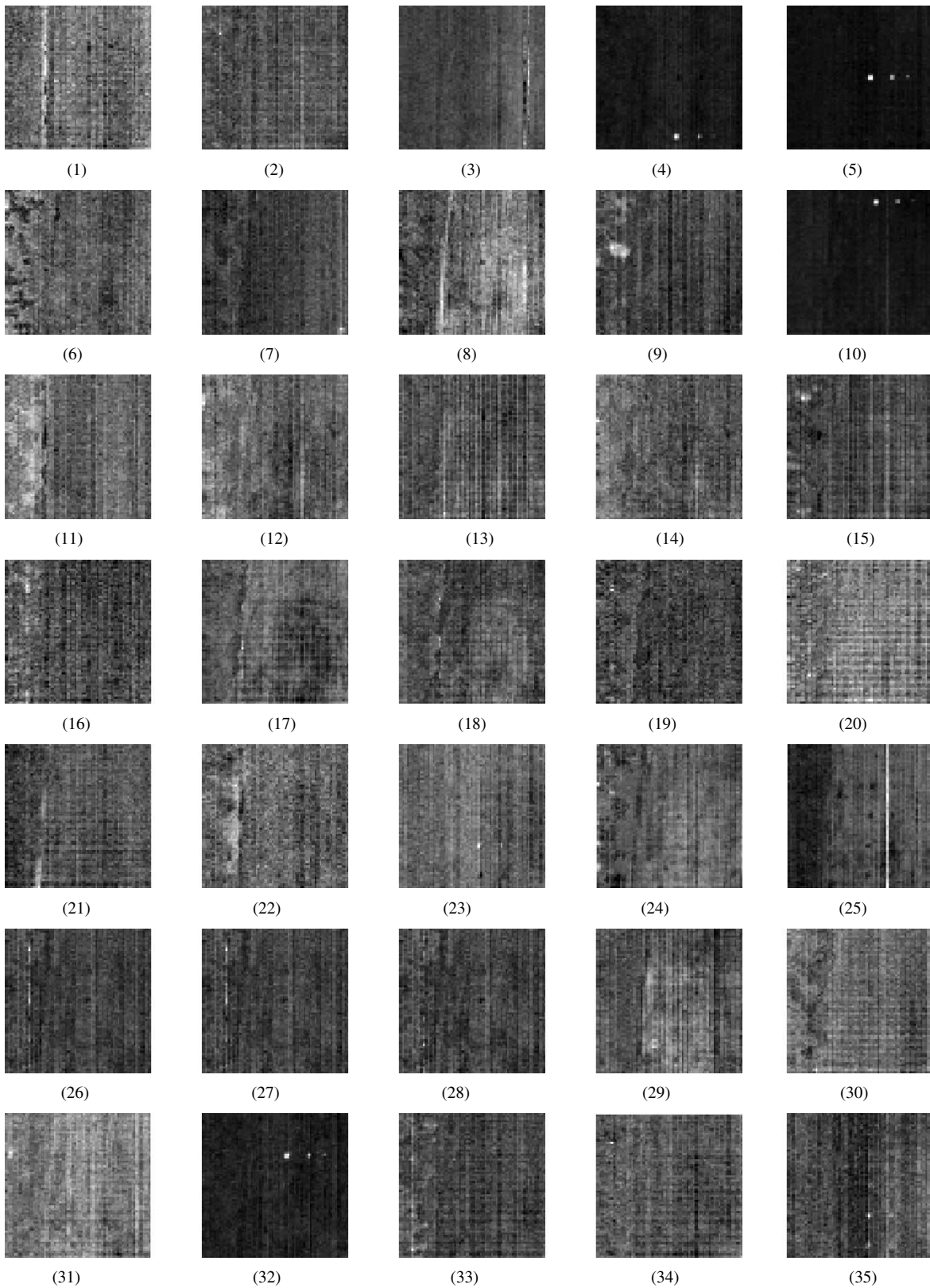


Fig. 10. Unsupervised classification results produced by the original uncompressed image for the HYDICE experiment.

four methods, where all of them produced comparable SNRs, PSNRs, but both the FCLSLU and UFCLSLU achieved CRs as high as 114:1 and 90:1, respectively, compared to 70:1 resulting from the LSLU and 57:1 from the PCA. Since the FCLSLU and the UFCLSLU are fully constrained, the dynamic

range of its produced fractional abundance images is $[0, 1]$. To the contrary, the LSLU has no constraints on abundance fractions. The range of its generated abundance values can be arbitrary. Table II tabulates the variances in abundance values resulting from the three methods, which show fully constrained

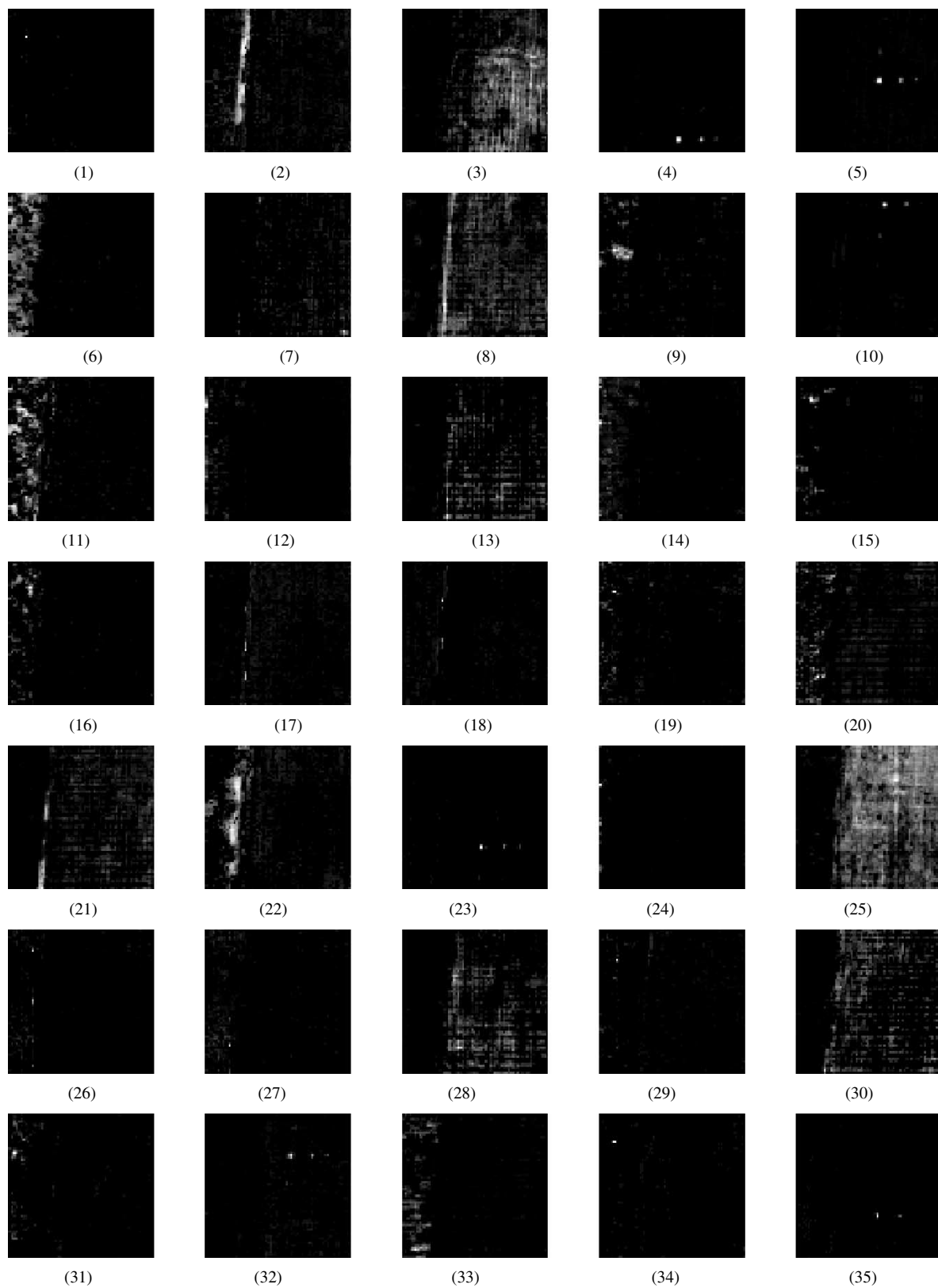


Fig. 11. Unsupervised classification results produced by the images reconstructed from the images reconstructed from 35 UFCLSLU-generated fractional abundance images for the HYDICE experiment.

methods yielded smaller variances than did an unconstrained method. Additionally, due to full abundance constraints, the FCLSLU and UFCLSLU only have to code $p - 1$ abundance fractional images compared to p abundance fractional images

needed for the LSLU. These advantages are the reasons that the FCLSLU and UFCLSLU could provide higher CRs. In our AVIRIS experiments, the FCLSLU provided a higher CR than did UFCLSLU, because the FCLSLU was only required to

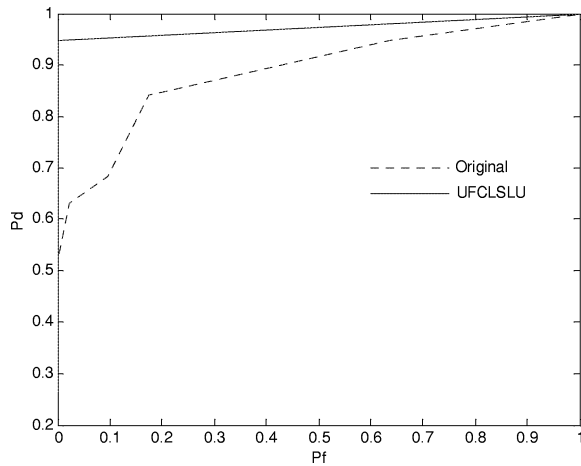


Fig. 12. ROC curves for the overall panel detection performance in Figs. 10 and 11.

code four fractional abundance images as opposed to five such images needed for the UFCLSLU.

We also conducted the experiments by using different round-off errors. Table III lists the results for the UFCLSLU. We can see that if the round-off error was 5×10^{-2} , the CR could be as high as about 240:1, but the SNR and PSNR were greatly decreased. If the round-off error was 5×10^{-4} , the CR was dramatically reduced to about 50:1 with slight increase on SNR and PSNR. The same phenomenon is observed for the PCA-, LSLU-, and FCLSLU-based compression. Therefore, 5×10^{-3} was a good choice in terms of compromise between CR and SNR (PSNR).

Fig. 3(a)–(d) shows the classification results produced by the original uncompressed images, the images reconstructed from the four PC images, and the LSLU- and FCLSLU-based compressed fractional abundance images, respectively, where five target signatures were directly extracted from the data by prior knowledge and used for compression. The classification was achieved using the OSP classifier in [20]. As shown, there is no visible difference between images in Fig. 3(a) and (c). The classified images in Fig. 3(b) from the PCA-based compression could not differentiate rhyolite and vegetation from each other. The images in Fig. 3(d) resulting from the FCLSLU seemed better than those in Fig. 3(a)–(c) in the sense that the effects caused by the interference and noise in image background were largely eliminated. Fig. 4(a) and (b) shows the classification results produced by the original uncompressed images and the images reconstructed from the UFCLSLU-based compressed fractional abundance images, respectively, where the same six target signatures (playa, shade, cinders, vegetation, rhyolite, anomaly) were used for the UFCLSLU. Interestingly, the classification results produced by the UFCLSLU-compressed images seemed better than those produced by original uncompressed images in terms of background compression, specifically, the classification of cinders, vegetation, and rhyolite. This was due to the fact that the anomaly had strong interference in target classification. Since it was included in the signature matrix used in the OSP classifier for annihilation, the resulting classification was significantly improved. This experiment demonstrated that unsupervised compression might produce better classification if

the used prior knowledge was incomplete. This is particularly true for hyperspectral imagery, where obtaining complete prior knowledge is generally difficult to obtain. From a classification point of view, both the LSLU-based and the UFCLSLU-based compression methods preserved the information of interest in the original image scene. However, the UFCLSLU-based compression performed better classification because imposing the ASC and ANC constraints provided more accurate abundance estimates.

Since there were five and six target signatures used to generate fractional abundance images for the LSLU and the UFCLSLU, we would wonder that the performance in Fig. 3(b) could be improved if five or six PC images rather than four PC images used for compression and decompression. The first five PC images and six PC images account for 99.89% and 99.90% energy, respectively. Surprisingly, this was not the case, as shown in Fig. 3(e) and (f). We still could not differentiate the vegetation from rhyolite as the same case shown in Fig. 3(b). However, the compression ratios of both cases were decreased to 46.79:1 and 39.93:1, respectively. This further demonstrated that the PCA-based compression suffered from preserving crucial information of small objects such as vegetation.

B. HYDICE Data Experiments

The HYDICE image data used in the following experiments is shown in Fig. 5(a) and (b), where band 10 ($0.5 \mu\text{m}$) and band 30 ($0.7 \mu\text{m}$) are included to demonstrate how the information provided by a band varies with its spectral coverage interval. It is of size 64×64 pixel vectors and has 15 panels in the scene. The low signal/high noise bands (bands 1–3 202–210) and water vapor absorption bands (bands 101–112 and 137–153) were removed. So, a total of 169 bands were used for the experiments. The spatial resolution is 1.5 m, and spectral resolution is 10 nm. As shown in Fig. 5(a), 15 panels are located in a large field and arranged in a 5×3 matrix compared to the scene in Fig. 5(b), which shows no sign of presence of these 15 panels. A ground truth map of these 15 panels in the image is given in Fig. 5(c) and provides the precise spatial locations of these 15 panels. Black pixels are panel center pixels, and the pixels in the white mask are panel pixels mixed with background pixels. Each element in this matrix is a square panel and denoted by p_{ij} with row indexed by $i = 1, 2, \dots, 5$ and column indexed by $j = 1, 2, 3$. For each row i , the three panels p_{i1}, p_{i2}, p_{i3} were painted by the same material but have three different sizes. For each column j , the five panels $p_{1j}, p_{2j}, p_{3j}, p_{4j}, p_{5j}$ have the same size but were painted by five different materials. The sizes of the panels in the first, second, and third columns are $3 \text{ m} \times 3 \text{ m}$, $2 \text{ m} \times 2 \text{ m}$, and $1 \text{ m} \times 1 \text{ m}$, respectively. The 1.5-m spatial resolution of the image scene suggests that except for $p_{21}, p_{31}, p_{41}, p_{51}$, which are two-pixel panels, all the remaining panels are only one pixel in size. This suggests that the 15 panels consist of 19 panel center pixels.

For the supervised LSLU-based compression, it is assumed that the knowledge of the 15 panels was available, where five panel signatures were generated by averaging the panel center pixels in each row, denoted by P_1, P_2, P_3, P_4 , and P_5 , respectively. Their spectra are shown in Fig. 5(d) and were used to for the target signature matrix \mathbf{M} . In the PCA-based compression,

TABLE VII
(a) TALLY OF THE NUMBER OF PANEL PIXELS DETECTED IN FIG. 10. (b) TALLY OF THE NUMBER OF PANEL PIXELS DETECTED IN FIG. 11(b)

	N _P	α = 0.1		α = 0.2		α = 0.3		α = 0.4		α = 0.5		α = 0.6		α = 0.7		α = 0.8		α = 0.9	
		N _D	N _F																
P1	3	3	2201	2	16	2	0	2	0	1	0	1	0	1	0	1	0	1	0
P2	4	4	3424	4	270	4	1	3	0	3	0	3	0	3	0	2	0	0	0
P3	4	4	598	4	0	4	0	3	0	3	0	2	0	2	0	2	0	2	0
P4	4	3	4050	3	3998	3	3540	2	1953	2	450	1	10	1	0	1	0	1	0
P5	4	4	2728	3	8	3	0	3	0	3	0	3	0	2	0	1	0	1	0
Total	19	18	13001	16	4292	16	3540	13	1953	12	450	10	10	9	0	7	0	5	0

(a)

	N _P	α = 0.1		α = 0.2		α = 0.3		α = 0.4		α = 0.5		α = 0.6		α = 0.7		α = 0.8		α = 0.9	
		N _D	N _F																
P1	3	3	5	2	1	2	0	2	0	1	0	1	0	1	0	1	0	1	0
P2	4	4	26	4	1	4	0	3	0	3	0	3	0	3	0	2	0	0	0
P3	4	4	2	4	1	4	0	3	0	3	0	2	0	2	0	2	0	2	0
P4	4	3	2	3	0	3	0	2	0	2	0	1	0	1	0	1	0	1	0
P5	4	4	1	3	0	3	0	3	0	3	0	3	0	2	0	1	0	1	0
Total	19	18	36	16	3	16	0	13	0	12	0	10	0	9	0	7	0	5	0

(b)

TABLE VIII
(a) CEM DETECTION RESULTS USING THE RECONSTRUCTED IMAGE FROM UFCLSLU-BASED COMPRESSION.
(b) CEM DETECTION RESULTS USING THE ORIGINAL IMAGE DATA

	N _P	α = 0.1		α = 0.2		α = 0.3		α = 0.4		α = 0.5		α = 0.6		α = 0.7		α = 0.8		α = 0.9	
		N _D	N _F																
P1	3	3	27	3	1	2	0	2	0	1	0	1	0	1	0	1	0	1	0
P2	4	4	349	4	6	4	0	3	0	2	0	1	0	1	0	0	0	0	0
P3	4	4	53	4	1	4	0	4	0	3	0	2	0	2	0	2	0	1	0
P4	4	4	45	4	2	3	0	2	0	2	0	1	0	1	0	1	0	1	0
P5	4	4	1	4	0	3	0	3	0	3	0	3	0	3	0	1	0	1	0
Total	19	19	475	19	10	16	0	14	0	11	0	8	0	8	0	5	0	4	0

	N _P	α = 0.1		α = 0.2		α = 0.3		α = 0.4		α = 0.5		α = 0.6		α = 0.7		α = 0.8		α = 0.9	
		N _D	N _F																
P1	3	3	1	3	0	2	0	2	0	1	0	1	0	1	0	1	0	1	0
P2	4	4	967	4	2	4	1	3	0	3	0	3	0	3	0	0	0	0	0
P3	4	4	82	4	0	4	0	3	0	3	0	2	0	2	0	1	0	1	0
P4	4	4	311	4	1	3	0	3	0	3	0	3	0	2	0	1	0	1	0
P5	4	4	66	4	0	3	0	3	0	3	0	3	0	1	0	1	0	1	0
Total	19	19	1427	19	3	16	1	14	0	13	0	12	0	9	0	4	0	4	0

the first nine PC images are used, which made up 99.93% energy, and the remaining PC images did not contain important target information. Table IV tabulates the SNRs, PSNRs, and CRs produced by the PCA-based, LSLU-based, and FCLSLU-based compression methods, where all the methods produced comparable SNRs and PSNRs but the FCLSLU achieved a much higher compression ratio 121:1 compared to 49:1 by the LSLU and 22:1 by the PCA. Fig. 6(a)–(d) shows the OSP classification results using the original 169 uncompressed band images, the images reconstructed from the PC images, the LSLU-generated fractional abundance images, and the FCLSLU fractional abundance images, respectively. As we can see from these images, the result in Fig. 6(d) was very different from those in Fig. 6(a)–(c), which were almost identical, and there was no visible difference among them. In order to conduct a quantitative study on panel detection, both grayscale OSP classification images were converted into binary images by normalizing the abundance fraction of each

image pixel to the range of [0, 1] and thresholding it using a threshold value γ between 0 and 1. Let N_D and N_F denote the total number of correctly detected pixels and total number of false-alarmed pixels, respectively. Table V(a)–(d) tallies the classification results of the 15 panels in Fig. 6(a)–(d) using various threshold values γ starting from 0.1–0.9 with an increment of 0.1. As we can see from Table V(a)–(c), the N_D and N_F obtained from Fig. 6(a)–(c) using the same threshold value γ were very close. In order to detect all the 19 panel center pixels, the threshold value γ must be small at the expense of very high false-alarm rates. For the false-alarm rate to be reduced, the threshold value γ must be set high, which will result in poor panel pixel detection. This is consistent with the classification images in Fig. 6(a)–(c), which contained a large number of background pixels. From Fig. 6(d) and Table V(d), all the panel pixels except those in row 2 could be detected with very small false-alarm rates compared to their counterparts produced in Fig. 6(a)–(c) and Table V(a)–(c). The

ROC curves based on Table V are plotted in Fig. 7, which describe the overall performance on the five different panel types. Obviously, the FCLSLU-based compression provides the best detection performance, while the detection using the PCA-based compression is the worst.

For unsupervised classification, no prior knowledge about the image scene was assumed. In this case, the UFCLSLU algorithm was conducted to locate targets of interest in an unsupervised manner to construct the target signature matrix \mathbf{M} in (1). Its SNR, PSNR, and CR were given in Table IV, where the UFCLSLU compression achieved the highest compression ratio, while its SNR and PSNR remained at a comparable level. Fig. 8(a) and (b) shows the OSP classification results using the fractional abundance images produced by the original 169 uncompressed band images and the images reconstructed from the UFCLSLU-based compression, respectively, where five target signatures generated by the UFCLSLU algorithm were used for the target signature matrix \mathbf{M} . Their results seemed to be close. However, unlike the supervised compression the 15 panels were classified into two separate images, the panels in the first three rows in one image and the panels in the last two rows in another image. Table VI(a) and (b) also tallies N_D and N_F for the unsupervised classification images in Fig. 8(a) and (b), respectively, using the threshold value γ from 0.1–0.9. Surprisingly, the OSP classification using the UFCLSLU-generated fractional abundance images performed slightly better than the OSP classification using original 169 uncompressed band images. For instance, when $\gamma = 0.2$, 18 out of 19 panel center pixels were correctly detected and classified by both methods. But the one using the UFCLSLU-generated fractional abundance images yielded $N_F = 90$ compared to $N_F = 104$ produced by the one using the original uncompressed image. The ROC curves plotted in Fig. 9 were very close. The area of $P_f = 0-0.1$ is enlarged for illustration. As shown, the curve from the UFCLSLU is slightly higher than that from the original image. The classification performance was further improved if the 35 targets generated by the UFCLSLU algorithm were used to form the target signature matrix \mathbf{M} for the OSP classification. Figs. 10 and 11 show the OSP classification results produced by the original 169 uncompressed band images and the UFCLSLU-generated fractional abundance images, respectively. The 15 panels in five rows were correctly detected and classified into five separate images as shown in Fig. 10 [10(4), 10(5), 10(10), 10(23), 10(32)] and Fig. 11 [11(4), 11(5), 11(10), 11(23), 11(32)] where the panels in row 5, row 3, row 1, row 4, and row 2 were detected, respectively. A quantitative comparison between Fig. 10(4) versus Fig. 11(4), Fig. 10(5) versus Fig. 11(5), Fig. 10(10) versus Fig. 11(10), Fig. 10(23) versus Fig. 11(23), Fig. 10(32) versus Fig. 11(32) was also conducted, and Table VII(a) and (b) tallies N_D and N_F for these unsupervised images. Their respective ROC curves are plotted in Fig. 12. The results of using the UFCLSLU-generated fractional abundance images were significantly better than that using the original uncompressed 169 band images. In Table VII(a) and (b), with the threshold γ being less than 0.3, the former detected 16 out of 19 panels with no false alarms compared to the same detection result with 3540 false-alarmed pixels produced by

the latter. In particular, comparing Fig. 11(23) to Fig. 10(23), there was significant improvement in detection of panels in row 4. The SNR, PSNR, and CR produced by the UFCLSLU method using 35 targets are also included in Table IV, where the CR was considerably reduced to 38 : 1, while the SNR and PSNR were moderately increased. This implies that the more target signatures generated, the better the classification, but the smaller the CR.

In order to further show the utility of our proposed UFCLSLU-based compression technique, the constrained energy minimization (CEM) [32] was also applied to both the original image of the 15-panel HYDICE scene and a UFCLSLU-based decompressed image to detect the five panel classes. The results are tabulated in Table VIII. As we can see, both results were comparable to each other. This experiment demonstrated that the UNFCLSLU-based compression was actually independent of algorithms to be used for target detection and classification.

For the experiments conducted in this paper, the computing time required for the UFCLSLU algorithm using a 440-MHz Sun workstation to run MATLAB codes on the AVIRIS data was 200 s, and 15 and 500 s for the HYDICE data using five signatures and 35 signatures, respectively.

VI. CONCLUSION

This paper presented an UFCLSLU-based spectral data compression technique for hyperspectral image analysis, where target detection and classification were used as a compression criteria. It first identified targets of interest in a hyperspectral image scene by an unsupervised process, then compressed the entire image cube to generate a set of fractional abundance images for these targets. In order to reliably estimate the target abundance fractions, the UFCLSLU method developed for material quantification in [22] and [27] was used to produce accurate target fractional abundance images. Several contributions are made in this paper. First, it developed an application exploited-based spectral compression technique for target detection and classification. Due to the fact that the number of targets of interest is generally much smaller than the number of spectral bands in hyperspectral imagery, a high compression ratio can be achieved. Second, since only fractional abundance images are encoded, unknown interfering sources including noise can be suppressed by compression. As a result, the performance analysis based on the target fractional abundance images can be improved over that produced by the original uncompressed images. Third, spatial correlation among pixels and variances in the UFCLSLU-generated fractional abundance images can, therefore, be substantially reduced, because most of the image background has been largely compressed, and only spatial redundancy among target pixels of interest remains to be removed, but will not be much. Accordingly, the gain resulting from spatial compression will be small. The coding redundancy can be removed by a simple entropy coding scheme, such as Huffman coding.

ACKNOWLEDGMENT

The authors would like to thank J. C. Harsanyi for providing the AVIRIS data.

REFERENCES

- [1] V. D. Vaughn and T. S. Wilkinson, "System considerations for multispectral image compression designs," *IEEE Signal Processing Mag.*, pp. 19–31, Jan. 1995.
- [2] J. A. Saghri, A. G. Tescher, and J. T. Reagan, "Practical transform coding of multispectral imagery," *IEEE Signal Processing Mag.*, pp. 32–43, Jan. 1995.
- [3] J. A. Saghri and A. G. Tescher, "Near-lossless bandwidth compression for radiometric data," *Opt. Eng.*, vol. 30, no. 7, pp. 934–939, July 1991.
- [4] J. A. Saghri, A. G. Tescher, and A. Boujarwah, "Spectral-signature-preserving compression of multispectral data," *Opt. Eng.*, vol. 38, no. 12, pp. 2081–2088, Dec. 1999.
- [5] G. P. Aboussleman, E. Gifford, and B. R. Hunt, "Enhancement and compression techniques for hyperspectral data," *Opt. Eng.*, vol. 33, no. 8, pp. 2562–2571, Aug. 1994.
- [6] G. P. Aboussleman, M. W. Marcellin, and B. R. Hunt, "Hyperspectral image compression using entropy-constrained predictive trellis coded quantization," *IEEE Trans. Image Processing*, vol. 6, pp. 566–573, Apr. 1994.
- [7] —, "Compression of hyperspectral imagery using the 3-D DCT and hybrid DPCM/DCT," *IEEE Trans. Geosci. Remote Sensing*, vol. 33, pp. 26–34, Jan. 1994.
- [8] S.-e. Qian, A. B. Hollinger, D. Williams, and D. Manak, "Fast three-dimensional data compression of hyperspectral imagery using vector quantization with spectral-feature-based binary coding," *Opt. Eng.*, vol. 35, no. 7, pp. 3242–3249, Nov. 1996.
- [9] R. O. Duda and R. E. Hart, *Pattern Classification and Scene Analysis*. New York: John Wiley & Sons, 1973.
- [10] J. A. Richards, *Remote Sensing Digital Image Analysis*, 2nd ed. Berlin, Germany: Springer-Verlag, 1993.
- [11] R. A. Schowengerdt, *Remote Sensing: Models and Methods for Image Processing*, 2nd ed. Orlando, FL: Academic, 1997, pp. 470–471.
- [12] B. B. Brower, D. H. Hadcock, J. P. Reitz, and J. Schott, "Spectrally and spatially adaptive hyperspectral data compression," *Proc. SPIE*, vol. 2821, pp. 55–63, 1996.
- [13] S. S. Shen and B. S. Beard, "Effects of hyperspectral compression on nonlinear exploitation," in *Proc. SPIE*, M. R. Descour and S. S. Shen, Eds., 1998, vol. 3438, pp. 191–199.
- [14] A. A. Green, M. Berman, P. Switzer, and M. D. Craig, "A transformation for ordering multispectral data in terms of image quality with implications for noise removal," *IEEE Trans. Geosci. Remote Sensing*, vol. 26, pp. 65–74, Jan. 1988.
- [15] J. B. Lee, A. S. Woodyatt, and M. Berman, "Enhancement of high spectral resolution remote sensing data by a noise-adjusted principal components transform," *IEEE Trans. Geosci. Remote Sensing*, vol. 28, pp. 295–304, May 1990.
- [16] C.-I Chang, Q. Du, T. S. Sun, and M. L. G. Althouse, "A joint band prioritization and band decorrelation approach to band selection for hyperspectral image classification," *IEEE Trans. Geosci. Remote Sensing*, vol. 37, pp. 2631–2641, Nov. 1999.
- [17] J. B. Adams, M. O. Smith, and A. R. Gillespie, "Image spectroscopy: Interpretation based on spectral mixture analysis," in *Remote Geochemical Analysis: Elemental and Mineralogical Composition*, C. M. Pieters and P. A. Englert, Eds. Cambridge, U.K.: Cambridge Univ. Press, 1993, pp. 145–166.
- [18] M. O. Smith, J. B. Adams, and D. E. Sabol, "Spectral mixture analysis—new strategies for the analysis of multispectral data," in *Image Spectroscopy—A Tool for Environmental Observations*, J. Hill and J. Mergier, Eds. Amsterdam, The Netherlands: Kluwer, 1994, pp. 125–143.
- [19] J. B. Farison, B. M. Cordell, and M. E. Shields, "AVIRIS image feature separation and image data compression and reconstruction," *Proc. SPIE*, vol. 3118, pp. 219–231, 1997.
- [20] J. C. Harsanyi and C.-I Chang, "Hyperspectral image classification and dimensionality reduction: An orthogonal subspace projection," *IEEE Trans. Geosci. Remote Sensing*, vol. 32, pp. 779–785, July 1994.
- [21] J. Bowles, D. Clamons, D. Gillis, P. Palmadesso, J. Antoniadis, M. Baumbach, M. Daniel, J. Grossmann, D. Haas, and J. Skibo, "New Results from the ORASIS/NEMO compression algorithm," in *Proc. SPIE*, M. R. Descour and S. Shen, Eds., 1999, vol. 3753, pp. 226–234.
- [22] C.-I Chang and D. Heinz, "Constrained subpixel target detection for remotely sensed images," *IEEE Trans. Geosci. Remote Sensing*, vol. 38, pp. 1144–1159, May 2000.
- [23] Y. E. Shimabukuro and J. A. Smith, "The least-squares mixing models to generate fraction images derived from remote sensing multispectral data," *IEEE Trans. Geosci. Remote Sensing*, vol. 29, pp. 16–20, Jan. 1991.
- [24] J. J. Settle and N. A. Drake, "Linear mixing and estimation of ground cover proportions," *Int. J. Remote Sens.*, vol. 14, no. 6, pp. 1159–1177, 1993.
- [25] E. A. Ashton and A. Schaum, "Algorithms for the detection of sub-pixel targets in multispectral imagery," *Photogramm. Eng. Remote Sens.*, pp. 723–731, July 1998.
- [26] D. Heinz, C.-I Chang, and M. L. G. Althouse, "Fully constrained least squares-based linear unmixing," in *Proc. IGARSS*, Hamburg, Germany, June 28–July 2 1999, pp. 1401–1403.
- [27] D. Heinz and C.-I Chang, "Fully constrained least squares linear mixture analysis for material quantification in hyperspectral imagery," *IEEE Trans. Geosci. Remote Sensing*, vol. 39, pp. 529–545, Mar. 2001.
- [28] Q. Du, C.-I Chang, D. C. Heinz, M. L. G. Althouse, and I. W. Ginsberg, "Hyperspectral image compression for target detection and classification," in *Proc. IGARSS*, July 24–28, 2000.
- [29] C. L. Lawson and R. J. Hanson, *Solving Least Squares Problems*. Philadelphia, PA: SIAM, 1995, vol. 15.
- [30] C. Brumbley and C.-I Chang, "An unsupervised vector quantization-based target signature subspace projection approach to classification and detection in unknown background," *Pat. Recognit.*, vol. 32, no. 7, pp. 1161–1174, July 1999.
- [31] H. Ren and C.-I Chang, "Automatic target recognition in hyperspectral imagery," *IEEE Trans. Aerosp. Electron. Syst.*, vol. 39, pp. 1232–1249, Oct. 2003.
- [32] J. C. Harsanyi, *Detection and Classification of Subpixel Spectral Signatures in Hyperspectral Image Sequences*. Baltimore, MD: Dept. Elect. Eng., Univ. Maryland, Aug. 1993.



Qian Du (S'98–M'00) received the Ph.D. degree in electrical engineering from the University of Maryland Baltimore County, Baltimore, in 2000.

She is currently an Assistant Professor in the Department of Electrical Engineering and Computer Science, Texas A&M University, Kingsville. Her research includes image processing, pattern classification, remote sensing, and neural networks.

Dr. Du is a member of SPIE and Phi Kappa Phi.



Chein-I Chang (S'81–M'87–SM'92) received the B.S. degree from Soochow University, Taipei, Taiwan, R.O.C., in 1973, the M.S. degree from the Institute of Mathematics, National Tsing Hua University, Hsinchu, Taiwan, in 1975, and the M.A. degree from the State University of New York, Stony Brook, in 1977, all in mathematics. He received the M.S. and M.S.E.E. degrees from the University of Illinois at Urbana-Champaign in 1982 and the Ph.D. degree in electrical engineering from the University of Maryland, College Park, in 1987.

He has been with the University of Maryland Baltimore County (UMBC), Baltimore, since 1987, as a Visiting Assistant Professor from January 1987 to August 1987, Assistant Professor from 1987 to 1993, Associate Professor from 1993 to 2001, and Professor in the Department of Computer Science and Electrical Engineering since 2001. He was a Visiting Research Specialist in the Institute of Information Engineering at the National Cheng Kung University, Tainan, Taiwan, from 1994 to 1995. He has a patent on automatic pattern recognition and several pending patents on image processing techniques for hyperspectral imaging and detection of microcalcifications. His research interests include automatic target recognition, multispectral/hyperspectral image processing, medical imaging, information theory and coding, signal detection and estimation, and neural networks. He is the author of a book *Hyperspectral Imaging: Techniques for Spectral Detection and Classification* (Norwell, MA: Kluwer). He is on the editorial board and was the Guest Editor of a special issue on telemedicine and applications of the *Journal of High Speed Networks*.

Dr. Chang received a National Research Council Senior Research Associateship Award from 2002–2003 at the U.S. Army Soldier and Biological Chemical Command, Edgewood Chemical and Biological Center, Aberdeen Proving Ground, MD. He is an Associate Editor in the area of hyperspectral signal processing for the IEEE TRANSACTION ON GEOSCIENCE AND REMOTE SENSING. He is a Fellow of SPIE and a member of Phi Kappa Phi and Eta Kappa Nu.